Available online at www.sciencedirect.com
SCIENCE DIRECT®
Journal of Nuclear Materials 343 (2005) 275–284
journal of nuclear materials
www.elsevier.com/locate/jnucmat

Tensile properties of candidate structural materials for high power spallation sources at high helium contents

P. Jung [a,*], J. Henry [b], J. Chen [a]

[a] *Institut für Festkörperforschung, Forschungszentrum Jülich, D-52425 Jülich, Germany*
[b] *CEA/DEN/SAC/DMN/SRMA, CEA Saclay, F-91191 Gif-sur-Yvette cedex, France*

Abstract

Low activation 9%Cr martensitic steels EUROFER97, pure tantalum, and low carbon austenitic stainless steel 316L were homogeneously implanted with helium to concentrations up to 5000 appm at temperatures from 70 °C to 400 °C. The specimens were tensile tested at room temperature and at the respective implantation temperatures. In all materials the helium caused an increased in strength and reduction in ductility, with both changes being generally larger at lower implantation and testing temperatures. After implantation some work hardening was retained in 316L and in tantalum, while it almost completely disappeared in EUROFER97. After tensile testing, fracture surfaces were analysed by scanning electron microscopy (SEM). Implantation caused reduction of necking, but up to concentrations of 2500 appm He fracture surface still showed transgranular ductile appearance. Completely brittle intergranular fracture was observed in tantalum at 9000 appm He and is also expected for EUROFER97 at this concentration, according to previous results on similar 9%Cr steels.

1. Introduction

In structural materials of high-power spallation sources, e.g. the European Spallation Source (ESS) or the Accelerator Driven System (ADS), hydrogen and helium are produced as major nuclear transmutation products at much higher rates than in fast-fission or fusion reactors [1]. While some of the hydrogen will escape, helium will be retained quantitatively and, due to its extremely low solubility, may cause severe degradation of material properties. A previous investigation on 9%Cr steels showed a strong increase in strength and reduction in ductility by implanted helium [2]. Especially at low temperatures, completely brittle fracture behaviour was observed for 5000 appm helium, which corresponds to about half year full power operation of ESS and ADS. It was the objective of the present work to study this effect of implanted helium in other materials, namely a reduced activation martensitic steel (EUROFER97) an austenitic stainless steel (316SS) and pure tantalum.

2. Experimental

2.1. Materials

The reduced activation martensitic steel EUROFER97 and the low carbon austenitic stainless steel IR316L were obtained from the European fusion materials programme. The major constituents (wt%, bal. Fe)

* Corresponding author. Tel.: +49 2461 614036; fax: +49 2461 614413.
E-mail address: p.jung@fz-juelich.de (P. Jung).

0022-3115/$ - see front matter © 2005 Elsevier B.V. All rights reserved.
doi:10.1016/j.jnucmat.2004.11.018

are for Eurofer97: C: 0.11, N: 0.03, P: 0.005, V: 0.2, Cr: 9.0, Mn: 0.48, Ni:0.021, Nb: 0.0017, Ta: 0.07, W: 1.1, and for IR316L: C: 0.056, N: 0.08, P: 0.02, Cr: 16.9, Mn: 1.65, Ni: 12.3, Mo: 2.45. Sheets of about 400 μm thickness were cut from the steel plates by spark erosion and were cold-rolled to 100 μm thickness in steps of 25% reduction, with intermediate annealing for 1 h at 750 °C (EUROFER97) and 0.5 h at 1040 °C (IR316L), respectively. Final heat treatment was 0.5 h at 980 °C – fast cooling – 1.5 h at 750 °C – slow cooling for EUROFER97 and 0.5 h at 1050 °C – fast cooling for IR316L, respectively. Tantalum was obtained as 100 μm thick foils of 99.9+ purity from ChemPur, Karlsruhe, and as 250 μm thick sheets of 99.9 purity from Goodfellow GmbH, Bad Nauheim. Gaseous impurity concentrations are N: 0.0003 and 0.0005, O: 0.0023 and 0.013, respectively, while for other impurities upper limits are C: < 0.001, V: < 0.005, Fe: < 0.005, Nb: < 0.01, Mo: < 0.01, W: < 0.02. The tantalum specimens were thinned after spark erosion to 88 μm and 180 μm, respectively, by grinding and polishing only. Dog bone shaped specimens of all materials were spark eroded to 28 mm total length, gauge sections of 10×2 mm, fillet radii of 1 mm and grips of 8×8 mm.

2.2. Implantation

In each implantation run, four specimens were mounted side by side, with only the lower grip fixed, while the upper one was free to avoid stresses from thermal expansion. One specimen had potential leads for resistance measurement. The maximum energy of α-particles (^{4}He) obtained from the Jülich compact cyclotron CV28 behind a 25 mm Hasteloy window is about 23.9 MeV. According to TRIM-SRIM calculations [3], this gives ranges ΔR of about 110 μm in steels and of 89 μm in tantalum, respectively. Homogeneous implantation throughout this thickness is achieved by using a degrader wheel with 24 Al foils of appropriate thickness which varies the energy in front of the specimens from 0 to 23.9 MeV [2]. Thickness of the degrader foils were optimised for steel to obtain inhomogeneity below 1%, giving a slightly higher value for Ta. Beam was scanned across the specimens at about 250/s, spreading more than 50% of the beam to a four-quadrant aperture to obtain fairly uniform distribution on the specimens. Uniformity of doses on the specimens was further improved by exchanging inner and outer specimens after half the total dose. Displacement production calculated by TRIM for implantation of 100 μm Fe and 88 μm Ta specimens is shown in Fig. 1. At the front side of the specimen, defect production is significantly higher, but, when specimens are turned around after reaching half the final dose, a fairly uniform damage distribution is obtained. With displacement energies T_d of 40 eV for steels and 88 eV for Ta [4], and a binding energy E_b of 2 eV for both materials, averages of 154 displacements per implanted ion are obtained for the steels and 69 for tantalum, corresponding to 0.66 and 1.45 at.% He/dpa, respectively. The T_d value for steel in the TRIM calculations was adopted from reactor irradiations, while experimental results for light ions suggest a higher value, i.e. lower displacement rates. These uncertainties in T_d (and E_b) are larger than differences between different steels, allowing to use Fe as a representative. Steel and tantalum specimens were implanted simultaneously. For a given beam current density, implantation rate is given by $\Phi/N_a\Delta R$, with Φ beam flux and N_a atomic density. The minor differences in N_a between different steels are nearly compensated by differences in ΔR. Typical implantation rates were about 0.015 appm He/s for steels and 0.029 appm He/s for Ta, corresponding to displacement rates of 2.3×10^{-6} and 2.0×10^{-6} dpa/s, respectively. Some ≈240 μm EUROFER97 and ≈180 μm thick tantalum specimens were implanted with ^{3}He ions of maximum energy 34 MeV, which have a maximum range of 242 μm in steels and 182 μm in Ta. In this case the average number of displacements per implanted ion is slightly lower, reaching 130 in steel and 60 in Ta, corresponding to 0.77 and 1.67 at.% He/dpa, respectively. Implantation rates in this case were about 0.006 appm/s for steels and 0.011 for Ta (0.71×10^{-6} and 0.65×10^{-6} dpa/s), respectively. Implantation dose was derived from measurements of beam current on a shutter during beam-off periods. Beam stability during implantation was monitored by the signals on the

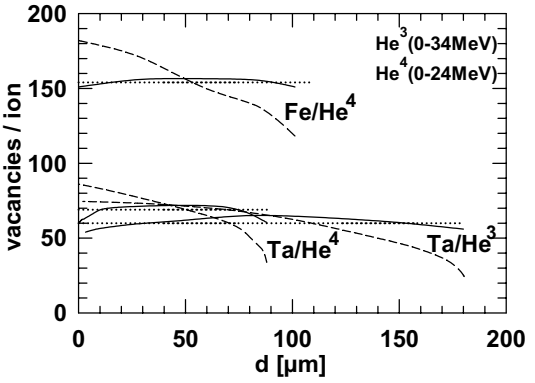

Fig. 1. Depth dependence of displacement damage produced by homogeneous implantation of $^4He^{++}$ ions (energies 0–24 MeV) in 100 μm iron (ρ = 7.87 g/cm^3, T_d = 40 eV, E_b = 2 eV) and in 88 μm tantalum (ρ = 16.6 g/cm^3, T_d = 88 eV, E_b = 2 eV), and of $^3He^{++}$ ions (energies 0–34 MeV) in 180 μm tantalum according to TRIM-SRIM calculations. Dashed curves correspond to implantation from front side, solid curves to specimens turned around after half the total dose, dotted lines to average value.

four-quadrant aperture. Implantation dose was derived from the beam current after correction for secondary electrons by about 30%, according to previous desorption experiments. Heating of the specimens was supplied only by the beam, with temperature adjustment by the flow rate of coolant. The specimens were cooled from both sides by flowing helium gas which gives at maximum flow rate a lower temperature limit of about 250 °C for the above implantation rates. Temperature was measured by infrared pyrometry under 45° from the backside of the specimens. Average temperature in the implanted area of one specimen was also obtained from four-point resistivity measurement. In an attempt to reach lower implantation temperatures, some specimens were soldered to a water-cooled heat sink by Wood's metal (T_m = 71 °C). Due to the poor thermal contact by this solder, temperature excursions above 71 °C could not be fully excluded. Production of transmutation products (e.g. H from α, p-reactions) is negligible in comparison to He implantation. Radioactivity of the implanted specimens is relatively low, allowing hands-on testing after about one week.

2.3. Tensile testing

The specimens were tensile tested in a testing device for miniature specimens, located in a vacuum furnace under 10^{-3} Pa. Testing was performed after evacuation and heating (<0.5 h) at a strain rate of 8.5×10^{-5}/s. Some tests at up to an order of magnitude higher strain rates showed no significant differences. Fracture surfaces were analysed by scanning electron microscopy (SEM) using a Hitachi S-4100 at a voltage of typically 20 kV. Reduction of area ($\Delta A/A$) of the foil specimens was approximated by the ratio of neck width (d_n) to total thickness d by

$$\Delta A/A = 1 - d_n/d. \quad (1)$$

3. Results

3.1. EUROFER97

Stress–strain curves of EUROFER97 before and after helium implantation at 250 °C are shown in Fig. 2 from tests at 25 °C and 250 °C. In general, stresses increase and strains decrease with increasing dose, and work-hardening is reduced up to about 1250 appm, where it virtually disappears and specimens become plastically unstable. Yield stresses ($\sigma_{0.2}$) and tensile stresses (σ_{UTS}) for various implantation and testing temperatures are summarised in Figs. 3 and 4. Figs. 5 and 6 show the strains at ultimate tensile strength (ε_{UTS}) and total elongation at fracture (ε_f), respectively. No significant effect of specimen thickness is observed for 100 μm and 240 μm (not include in the figures) specimens. Generally the increase in strength and decrease in strain is higher at lower temperatures down to 250 °C, while no substantial differences in results are observed between 250 °C and 150 °C (see 1250 appm data). Numerical

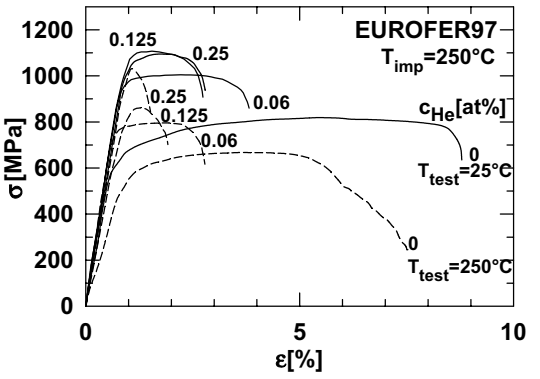

Fig. 2. Stress–strain curves of EUROFER97 after implantation at 250 °C to various He concentrations, tested at a strain rate of 8.5×10^{-5}/s at 25 °C (solid) and 250 °C (dashed), respectively. The temperature of the 2500 appm implantation was possibly slightly above 250°C.

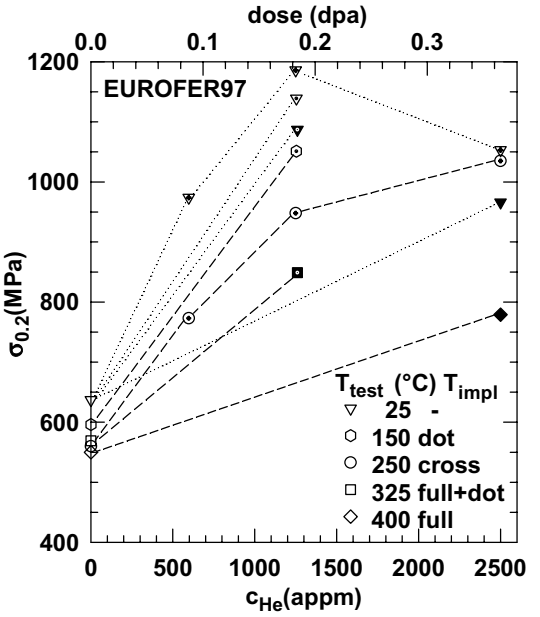

Fig. 3. Yield stress $\sigma_{0.2}$ of EUROFER97 as a function of helium concentration at various implantation and testing temperatures. The upper axis gives displacement dose as derived from Fig. 1 for ^{4}He. Dotted lines connect tests at RT, dashed lines those performed at respective implantation temperatures.

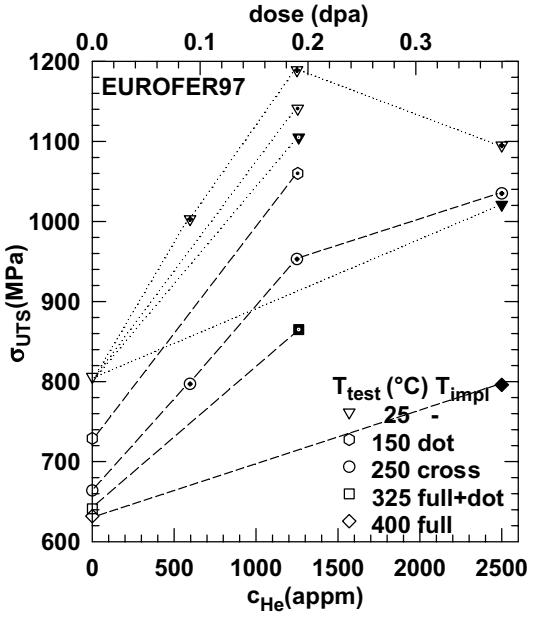

Fig. 4. Tensile stresses σ_{UTS} of EUROFER97 as a function of helium concentration at various implantation and testing temperatures. The upper axis gives displacement dose as derived from Fig. 1 for ^{4}He. Dotted lines connect tests at RT, dashed lines those performed at respective implantation temperatures.

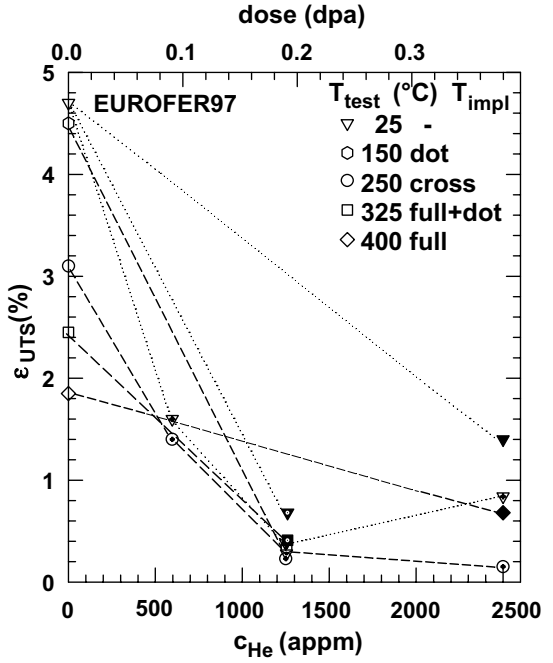

Fig. 5. Elongation at σ_{UTS} of EUROFER97 as a function of helium concentration at various implantation and testing temperatures. The upper axis gives displacement dose as derived from Fig. 1 for ^{4}He. Dotted lines connect tests at RT, dashed lines those performed at respective implantation temperatures.

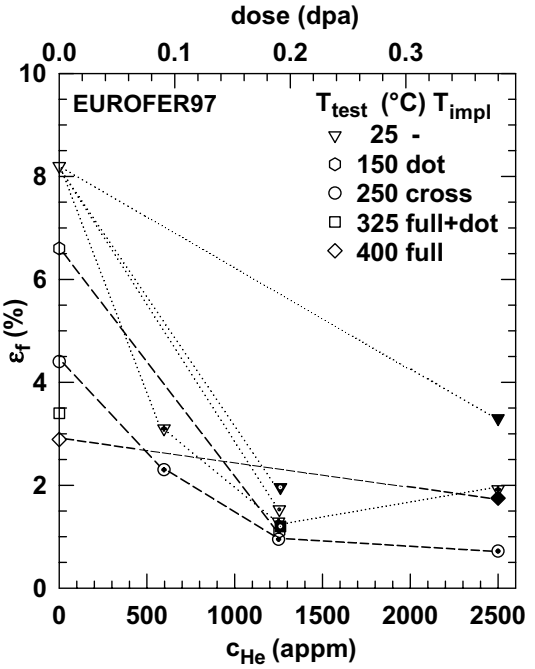

Fig. 6. Total elongation ε_f of EUROFER97 as a function of helium concentration at various implantation and testing temperatures. The upper axis gives displacement dose as derived from Fig. 1 for ^{4}He. Dotted lines connect tests at RT, dashed lines those performed at respective implantation temperatures.

data are given in Table 1. Uniform strain and stress parameters can be empirically correlated by

$$\varepsilon_{UTS} = 0.15(1 - \sigma_{0.2}/\sigma_{UTS})^{0.8}. \quad (2)$$

A semi-empirical model [5] suggests a linear relation which gives only poor agreement for the EUROFER97 data (prefactor: 0.2), while agreement is satisfactory for T91 [2] (prefactor: 0.3).

Fracture surfaces from SEM after implantation at 250 °C and testing at room temperature are shown in Fig. 7 for two different magnifications. The upper pictures show the reduction of necking with dose, while the lower enlarged pictures show a gradual transition from a ductile dimple type fracture to an increasingly coarser fracture appearance. Reduction of area ($1-d_n/d$) after implantation at 250 °C and testing at 25 °C as well as at 250 °C shows a sharp drop at concentrations below 600 appm He from about 0.8 to 0.58, and then remains virtually constant up to 0.25 at.%, analogous to the behaviour of strains in Figs. 5 and 6. At higher implantation temperature, the decrease is more gradual. This behaviour of A/A is similar to results from T91 [2], which also showed a plateau between about 600 appm and 2500 appm He, while a second strong decrease was found there between 2500 appm and 5000 appm He, associated with a transition to brittle intergranular fracture.

Table 1
Specimen thickness d, implantation temperature T_{impl} and dose c_{He}, testing temperature T_{test} and tensile data of tested specimens

Spec. no.	d [μm]	T_{impl} [°C]	c_{He} [appm]	T_{test} [°C]	$\sigma_{0.2}$ [MPa]	σ_{UTS} [MPa]	ε_{UTS} [%]	ε_t [%]	d_n/d
EUROFER97									
116/E1	105	–	0	25	637	806	4.70	8.20	0.26
123/E1	105	–	0	150	596	729	4.50	6.60	0.23
184/E3	101	–	0	250	560	664	3.10	4.40	0.20
177/E3	101	–	0	325	569	641	2.45	3.40	0.27
120/E1	104	–	0	400	550	632	1.85	2.89	0.20
115/E1	103	150	1250	25	1139	1141	0.28	1.53	0.25
117/E1	102	150	1250	150	1051	1060	0.34	1.10	0.31
118/E1	103	250	625	25	974	1003	1.60	3.10	0.43
119/E1	103	250	625	250	773	797	1.40	2.30	0.30
180/E3	100	250	1250	25	1186	1189	0.38	1.29	0.41
181/E3	100	250	1250	250	948	953	0.23	0.95	0.41
178/E3	102	250	2500	25	1053	1095	0.84	1.92	0.42
126/E2	237	250	2500	25	1152	1182	0.58	1.50	0.43
179/E3	101	250	2500	250	1035	1035	0.15	0.72	0.39
127/E2	237	250	2500	250	960	974	0.51	0.72	0.68
121/E1	102	325	1250	25	1087	1105	0.68	1.96	0.25
122/E1	104	325	1250	325	849	865	0.41	1.20	0.30
124/E1	101	400	2500	25	966	1021	1.40	3.30	0.34
125/E1	101	400	2500	400	779	796	0.68	1.75	0.36
Tantalum									
166/R1	90	–	0	25	236	362	25.1	28.6	$\leqslant$0.05
132/R2	181	–	0	25	233	343	25.2	29.2	$\approx$0.40
167/R1	91	–	0	200	198	327	12.0	13.3	$\approx$0.00
133/R2	176	–	0	250	176	396	18.3	20.9	0.22
163/R1	89	<70	1700	25	655	862	6.2	7.7	$\leqslant$0.06
164/R1	90	200	9200	25	687	812	1.56	1.95	0.92
165/R1	90	200	9200	200	546	635	1.2	1.67	0.41
130/R2	178	250	5100	25	666	800	3.4	4.7	0.50
131/R2	181	250	5100	250	572	685	1.28	2.3	$\approx$0.00
IR316L									
112/A1	102	–	0	25	204	589	49.9	51.7	$\leqslant$0.13
110/A1	104	–	0	250	125	400	24.1	27.0	$\leqslant$0.06
106/A1	103	250	2400	25	586	826	11.3	12.5	$\leqslant$0.125
107/A1	102	250	2400	250	610	694	3.2	3.7	$\leqslant$0.25
113/A1	103	250	4900	25	686	1066	7.8	8.2	$\leqslant$0.24
114/A1	102	250	4900	250	476	785	5.8	6.0	$\leqslant$0.06

3.2. Tantalum

Stress–strain curves of pure tantalum after implantation at 250 °C to 5100 appm ^{3}He and at 200 °C to 9200 appm ^{4}He, tested at a strain rate of 8.5×10^{-5}/s at 25 °C and at the respective implantation temperature are shown in Fig. 8. Numerical data are included in Table 1. General behaviour is similar to EUROFER97 with the exception that no plastic instability is observed up to the highest concentration. Tensile properties $\sigma_{0.2}$, σ_{UTS}, ε_{UTS}, and ε_f at various implantation and testing temperatures are summarised in Figs. 9 and 10. The data base is insufficient to derive detailed dependences on concentration and temperature, but it is obvious that similar to EUROFER97, after a strong change in properties below about 1000 appm He, stresses (Fig. 9) show only minor changes up to 9200 appm He, while strains (Fig. 10) still gradually decrease. Fracture surfaces from SEM after implantation at 200 °C and 250 °C and testing at room temperature are shown in Fig. 11. Also a reduction of necking is observed at increasing concentration, with a large fraction of intergranular brittle fracture at 9200 appm He.

3.3. IR316L

Stress–strain curves of IR316L after implantation at 250 °C to 2400 appm He and 4900 appm He, tested at a strain rate of 8.5×10^{-5}/s at 25 °C and 250 °C, respectively, are shown in Fig. 12. For numerical data see

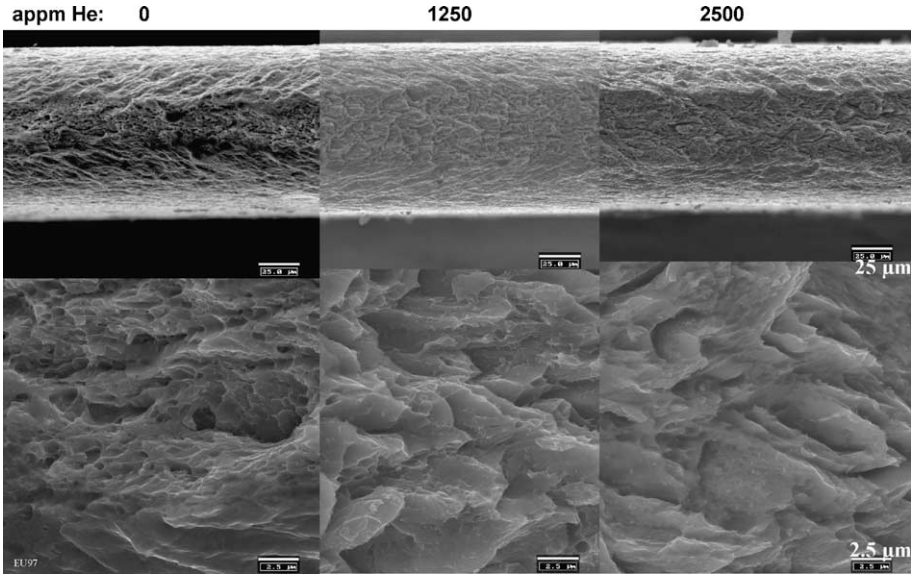

Fig. 7. SEM micrographs of EUROFER97, implanted at 250 °C to He concentrations of 0, 1250, and 2500 appm, after tensile testing at 25 °C.

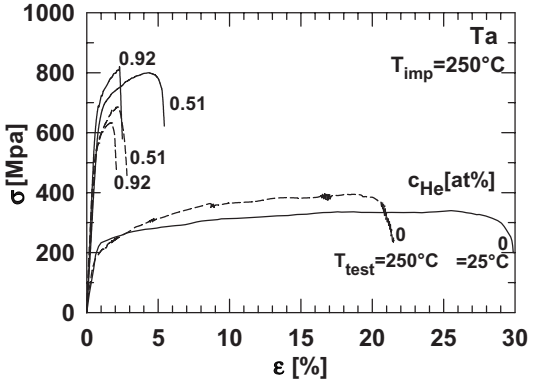

Fig. 8. Stress-strain curves of pure tantalum after implantation at 250 °C to 5100 appm He and at 200 °C to 9200 appm He, tested at a strain rate of 8.5×10^{-5}/s at 25 °C (solid) and at implantation temperature (dashed), respectively.

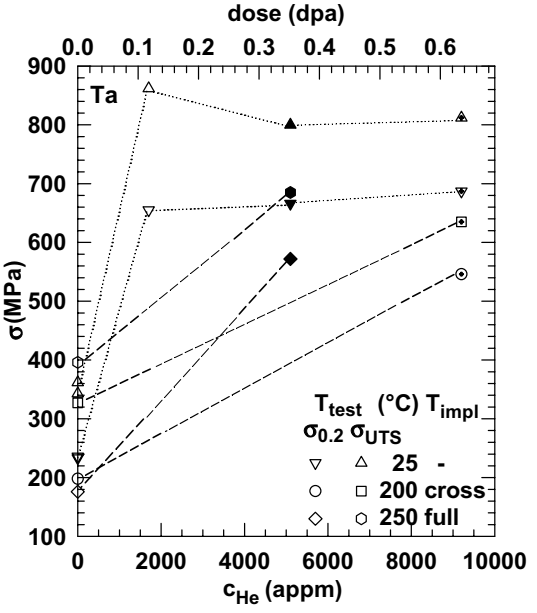

Fig. 9. Yield stress $\sigma_{0.2}$ and tensile stresses σ_{UTS} of tantalum as a function of helium concentration at various implantation and testing temperatures. The upper axis gives displacement dose as derived from Fig. 1 for ^{4}He. Dotted lines connect tests at RT, dashed lines those performed at respective implantation temperatures.

Table 1. Also in 316 L, the stresses increase and the strains decrease with increasing dose, but work hardening is retained up to the highest concentration of 4900 appm He. Yield stresses $\sigma_{0.2}$ and tensile stresses σ_{UTS} for various implantation and testing temperatures are summarised in Fig. 13. Both show significant increase even between 2400 appm and 4900 appm He, at least in the tests at 25 °C. Fig. 14 shows the strains at ultimate tensile strength (ε_{UTS}) and total elongation at fracture (ε_f), respectively. Both ε_{UTS} and ε_f continue to decrease from 2400 appm to 4900 appm He when tested at 25 °C, while testing at 250 °C gives an increase in this dose regime. Fracture surfaces from SEM after implantation at 250 °C and testing 25 °C and 250 °C are shown in Fig. 15. Almost complete necking is observed up to

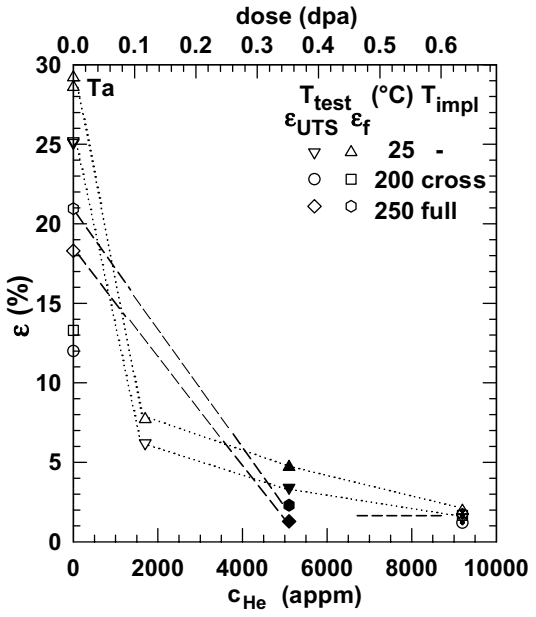

Fig. 10. Elongation at ε_{UTS} and total elongation ε_f of tantalum as a function of helium concentration at various implantation and testing temperatures. The upper axis gives displacement dose as derived from Fig. 1 for ^{4}He. Dotted lines tentatively indicate the trends of ε_{UTS} and ε_f after implantation at 200 °C/250 °C and testing at 25°C, respectively. Dotted lines connect tests at RT, dashed lines those performed at respective implantation temperatures.

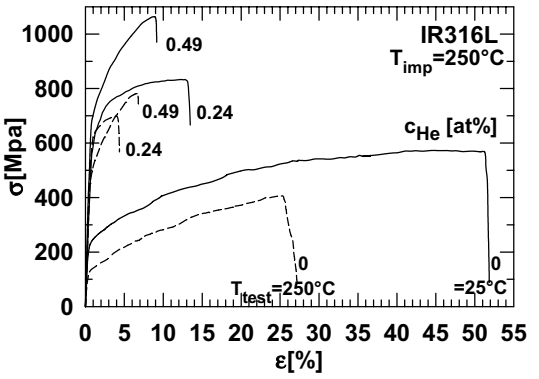

Fig. 12. Stress-strain curves of IR316L after implantation at 250 °C to 2400 appm He and 4900 appm He, tested at a strain rate of 8.5×10^{-5}/s at 25 °C (solid) and 250 °C (dashed), respectively.

the highest concentration, with only narrow areas of dimple fracture appearance.

4. Discussion

Three topics will be addressed:

(1) Dose dependence of strengths and strains in EUROFER97.

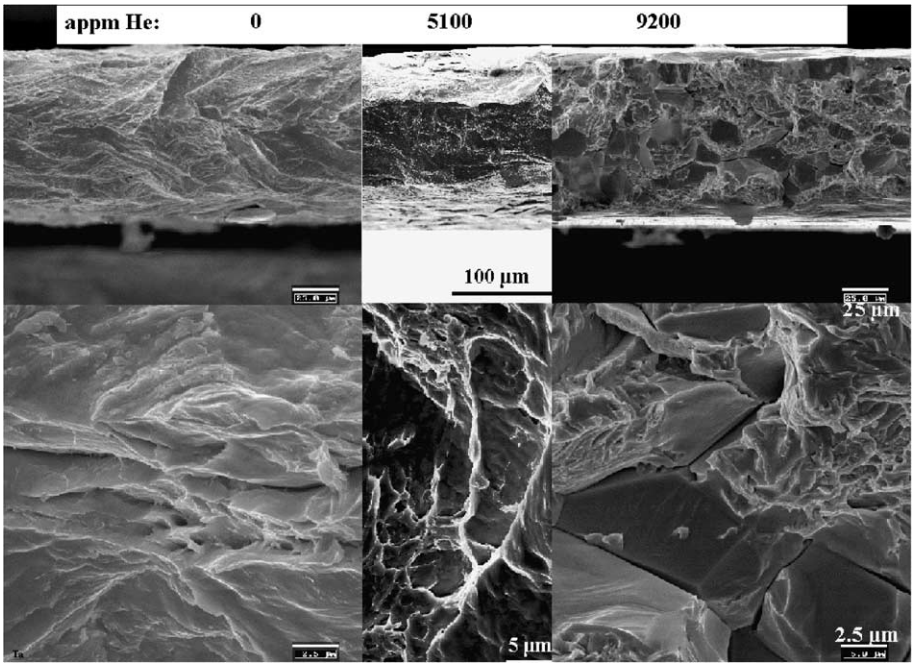

Fig. 11. SEM micrographs of fracture surfaces of unimplanted tantalum (thickness 88 μm), of specimens implanted at 250 °C to 5100 appm ^{3}He (178 μm) and at 200 °C to 9200 appm ^{4}He (88 μm), after tensile testing at 25°C.

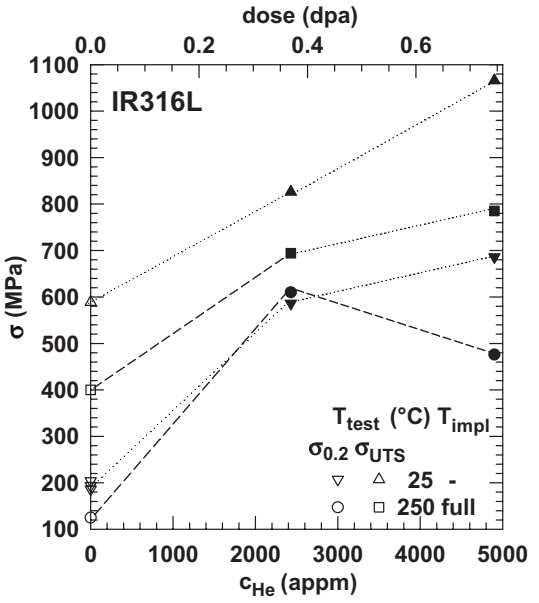

Fig. 13. Yield stress $\sigma_{0.2}$ and tensile stresses σ_{UTS} of IR316L as a function of helium concentration at various implantation and testing temperatures. The upper axis gives displacement dose as derived from Fig. 1 for ^{4}He. Dotted lines connect tests at RT, dashed lines those performed at respective implantation temperatures.

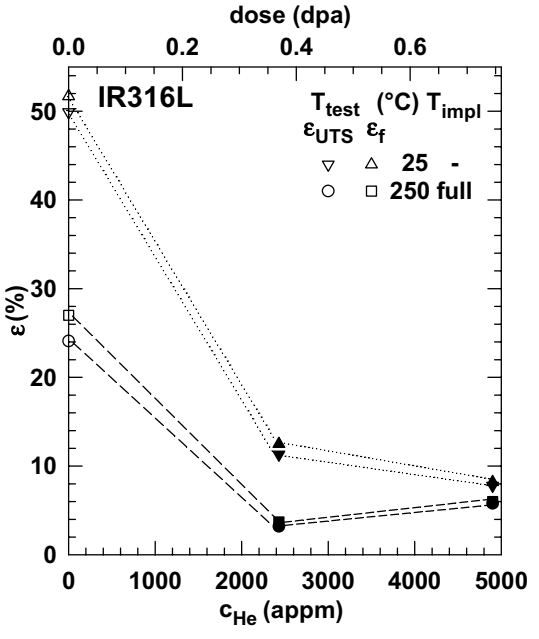

Fig. 14. Elongation at ε_{UTS} and total elongation ε_f of IR316L as a function of helium concentration at various implantation and testing temperatures. The upper axis gives displacement dose as derived from Fig. 1 for ^{4}He. Dotted lines connect tests at RT, dashed lines those performed at respective implantation temperatures.

(2) Comparison of the present results of implanted EUROFER97 to irradiation in reactors and spallation sources.
(3) Change in fracture mode at high helium concentrations.

After implantation at 250 °C, EUROFER97 (Figs. 3–6) shows a strong change in dose dependence of both yield- and tensile strength at concentrations above 1250 appm He (0.19 dpa). This change of strength parameters is associated with a corresponding change of ductility parameters, namely from a strong decrease at doses below 1250 appm He to a much lesser decrease above. This behaviour becomes more clear when the implantation induced change of yield stress is plotted according to a power law

$$\Delta\sigma_{0.2} = \sigma'(\Phi)^n \tag{3}$$

and tensile strain by a logarithmic law

$$\ln(\varepsilon_0/\varepsilon_{UTS}) = \Phi/\Phi' \tag{4}$$

with $\varepsilon_0 = \varepsilon_{UTS}(0)$. Parameters σ', n, ε_0 and Φ' for the low dose regime (<0.19 dpa) are given in Table 2. Included are results from He-implanted T91 [2] and from reactor (HFIR) irradiation [6], where similar behaviour has been observed. Table 2 gives remarkably uniform values of $n \approx 0.7 \pm 0.15$ and $\Phi' \approx 0.07 \pm 0.02$ after He implantation and reactor irradiation. Also hydrogen implantations [7,8], which are limited to very low doses of about 0.03 dpa, give similar values of n. If strength is ascribed to the combined effect of pre-existing dislocations (obstacle strength coefficient α_d, line density ρ_d) and irradiation induced defects (α_l, ρ_l, where ρ_l is set equal to $N_l d_l$ in the case of loops, with N_l number density and d_l diameter) their respective contributions can be described by (cf. [9]):

$$\Delta\sigma_{0.2,i} \propto \rho_i^{1/2} \quad i = \{l, d\}. \tag{5}$$

Superposition of both contributions by a linear ($\Delta\sigma_{0.2} = \Sigma\Delta\sigma_{0.2,i}$) or by a square law ($\Delta\sigma_{0.2}^2 = \sum\Delta\sigma_{0.2,i}^2$) gives at very low doses when dislocations still dominate: $\Delta\sigma_{0.2} \propto \alpha_l \cdot \rho_l^{1/2}$ and $\Delta\sigma_{0.2} \propto \alpha_l^2\rho_l/2\alpha_d\rho_d^{1/2}$, respectively. With the experimentally observed constancy of N_l and linear dose dependence of d_l [10] (for austenitics see [11,12]), giving a linear dependence on ρ_l, one expects values of n between 0.5 (linear law) and 1 (square law), in agreement with the results of Table 2. n values above 0.5 could also be attained, even in the case of linear superposition, by an increase of α_l with dose, when loops start to grow. At slightly higher doses, when the irradiation induced defects (loops) become dominant (and α_l is constant) $n = 0.5$ prevails. The agreement between the results in the 9Cr steels from He implantation and neutron irradiation shows that hardening and loss of ductility in the very low dose regime is dominated by displacement damage. The result

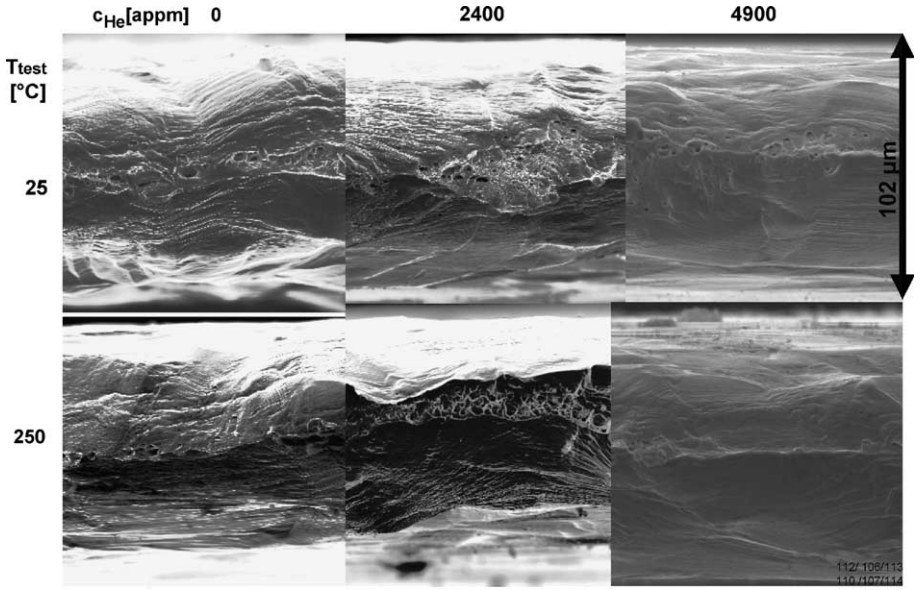

Fig. 15. SEM micrographs of fracture surfaces of unimplanted IR316L, and of specimens implanted at 250 °C to 2400 appm He and 4900 appm He.

Table 2
Comparison of the dependence of $\Delta\sigma_{0.2}$ and $\Delta\varepsilon_{UTS}$ of 9%Cr steels on displacement dose Φ [dpa] below about 0.05 dpa under various irradiation conditions

Material	Irradiation/ implantation	$T_{irr/impl}$ [°C]	T_{test} [°C]	$\Delta_{0.2} = \sigma'(\Phi)^n$		$\ln(\varepsilon 0/\varepsilon_{UTS}) = \Phi/\Phi'$		Ref.
				σ' [MPa]	n	ε_0 [%]	Φ'[dpa]	
EU97	He-implantation	250	25	1640	0.66	4.3	0.079	This work
EU97	He-implantation	250	250	1510	0.83	3.0	0.074	This work
T91	He-implantation	250	25	1025	0.55	5.9	0.088	[2]
T91	He-implantation	250	250	1445	0.78	3.9	0.123	[2]
EU97	H-implantation	<70°C	25	1460	0.76	5.2	0.058	[7]
F82H-mod	H-implantation	<70°C	30	2060	0.65	4.8	0.049	[8]
9Cr1MoVNb	Neutrons (HFIR)	60–100	25	1850	0.60	6.2	0.050	[6]

that helium has only a minor effect on tensile properties at low doses is corroborated by the good agreement between results after irradiation in reactor and spallation source [6] considering their large difference in helium production. The only difference being the extension of this regime to higher doses and higher $\Delta\sigma_{0.2}$ values under He implantation.

The decrease of n and the levelling-off of ε_{UTS} at higher doses agrees qualitatively with results from irradiations in HFIR [6] ($n = 0.11$) and in LANSCE. In the latter case values of $n = 0.24$ and 0.27 can be evaluated from the data given in [13] and [14], respectively. A possible explanation of this decrease of n is reduced interaction of the obstacles, e.g. by loop reorientation or by flux localisation (e.g. dislocation channelling, as tentatively proposed in [6]). Up to now, a microstructural proof of this explanation is missing. An alternative explanation would be a decrease of the effective strength α_l of obstacles. In the case of small loops, strength contribution is assumed to increase with size, but it may decrease when large loops tend to entangle into the network. In this dose regime the increase in yield stress of EUROFER97 as well as T91 after He implantation are significantly higher than after HFIR [6] or LANSCE [14] irradiation when compared on dpa basis. A better agreement with the LANSCE data – but not with the HFIR data – is obtained when compared on basis of helium content [2]. Enhanced loop growth by helium as indicated in [15] could explain this result.

Fracture surfaces of EUROFER97 show no significant changes in the low dose regime (Fig. 7). On the other hand, T91 shows a transition to partially intergranular fracture between 2400 appm and 5000 appm He [2]. From this result on T91 a similar behaviour, i.e. intergranular fracture above 2500 appm He may be expected for EUROFER97. This transition in the steel

corresponds to a displacement dose below 0.75 dpa. Such dramatic behaviour has never been observed after irradiations in reactors or spallation sources even at much higher displacement doses, but much lower accumulated helium concentrations (maximum 1500 appm He [16]). Also bcc-tantalum shows between 5100 appm and 9200 appm He a dramatic transition to partially intergranular fracture, almost without necking after implantation at 250 °C and testing at 25 °C (Fig. 11). In 316 L, such a transition in fracture mode was not observed at a He concentration up to 5000 appm, but has been reported at 10,000 appm for testing at 25 °C [15]. In these high concentrations, also additional hardening by implanted helium has been observed [17].

5. Conclusions

1. Comparison of results from He implantation and neutron irradiation of 9Cr steels indicates that hardening and ductility loss at low doses is dominated by displacement damage.
2. At higher He concentrations transition of fracture mode to intergranular brittle behaviour is observed, namely between 2400 and 5000 appm He in 9Cr steels, between 5100 and 9200 appm He in tantalum, and probably above 5000 appm He in austenitic 316 L.
3. Microstructure of implanted material needs investigation to understand the particular effects of helium on strength and ductility.
4. Bending, impact, or small-punch experiments, may give insight in changes of fracture mode induced by helium at high concentrations.
5. Synergy effects with hydrogen, which is produced in even higher amounts, should be studied by co-implantation.

References

[1] P. Jung, J. Phys. IV, France 12 (2002) Pr8-59.
[2] P. Jung, J. Henry, J. Chen, J.-C. Brachet, J. Nucl. Mater. 318 (2003) 241.
[3] J.P. Biersack, L.G. Haggmark, Nucl. Instrum. and Meth. 174 (1980) 93;
J.F. Ziegler, Manual of TRIM Version 95.4, March 1995, unpublished.
[4] P. Jung, Phys. Rev. B 23 (1981) 664.
[5] G.R. Odette, D. Frey, J. Nucl. Mater. 85&86 (1979) 817.
[6] K. Farrell, T.S. Byun, J. Nucl. Mater. 318 (2003) 274.
[7] C. Liu, H. Klein, P. Jung, J. Nucl. Mater. 335 (2004) 77.
[8] P. Jung, C. Liu, J. Chen, J. Nucl. Mater. 296 (2001) 165.
[9] G.E. Lucas, J. Nucl. Mater. 206 (1993) 287.
[10] X. Jia, Y. Dai, J. Nucl. Mater. 318 (2003) 207.
[11] Y. Dai, X. Jia, J.C. Chen, W.F. Sommer, M. Victoria, G.S. Bauer, J. Nucl. Mater. 296 (2001) 174.
[12] B.H. Sencer, G.M. Bond, M.L. Hamilton, F.A. Garner, S.A. Maloy, W.F. Sommer, J. Nucl. Mater. 296 (2001) 112.
[13] K. Farrell, T.S. Byun, J. Nucl. Mater. 296 (2003) 129.
[14] M.B. Toloczko, M.L. Hamilton, S.A. Maloy, J. Nucl. Mater. 318 (2003) 200.
[15] H. Ullmaier, J. Chen, J. Nucl. Mater. 318 (2003) 228 (and private communication).
[16] J. Chen, G.S. Bauer, T. Broome, F. Carsughi, Y. Dai, S.A. Maloy, M. Roedig, W.F. Sommer, H. Ullmaier, J. Nucl. Mater. 318 (2003) 56.
[17] J.D. Hunn, E.H. Lee, T.S. Byun, L.K. Mansur, J. Nucl. Mater. 296 (2001) 203.